Two-axis magnetically-driven MEMS scanning catheter for endoscopic high-speed optical coherence tomography

Ki Hean Kim[1], B. Hyle Park[1], Gopi N. Maguluri[1], Tom W. Lee[2], Fran J. Rogomentich[2], Mirela G. Bancu[2], Brett E. Bouma[1], Johannes F. de Boer[1], and Jonathan J. Bernstein[2*]

[1]Wellman Center for Photomedicine, Massachusetts General Hospital, Boston, MA 02114 USA
[2]Charles Stark Draper Laboratory, Cambridge, MA 02139 USA
**Corresponding author: jbernstein@draper.com*

Abstract: A two-axis scanning catheter was developed for 3D endoscopic imaging with spectral domain optical coherence tomography (SD-OCT). The catheter incorporates a micro-mirror scanner implemented with microelectromechanical systems (MEMS) technology: the micro-mirror is mounted on a two-axis gimbal comprised of folded flexure hinges and is actuated by magnetic field. The scanner can run either statically in both axes or at the resonant frequency (>= 350Hz) for the fast axis. The assembled catheter has an outer diameter of 2.8 mm and a rigid part of 12 mm in length. Its scanning range is ± 20˚ in optical angle in both axes with low voltages (1~3V), resulting in a scannable length of approximately 1 mm at the surface in both axes, even with the small catheter size. The catheter was incorporated with a multi-functional SD-OCT system for 3D endoscopic imaging. Both intensity and polarization-sensitive images could be acquired simultaneously at 18.5K axial scans/s. *In vivo* 3D images of human fingertips and oral cavity tissue are presented as a demonstration.

OCIS codes: (170.4500) Optical coherence tomography; (170.2150) Endoscopic imaging; (350.3950) Micro-optics; (110.6880) Three-dimensional acquisition

References and links

1. D. Huang, E. A. Swanson, C. P. Lin, J. S. Schuman, W. G. Stinson, W. Chang, M. R. Hee, T. Flotte, K. Gregory, C. A. Puliafito, and J. G. Fujimoto, "Optical coherence tomography," Science **254,** 1178-1181 (1991).
2. J. G. Fujimoto, "Optical coherence tomography for ultrahigh resolution in vivo imaging," Nat. Biotechnol. **21,** 1361-1367 (2003).
3. J. S. Schuman, M. R. Hee, A. V. Arya, T. Pedut-Kloizman, C. A. Puliafito, J. G. Fujimoto, and E. A. Swanson, "Optical coherence tomography: a new tool for glaucoma diagnosis," Current opinion in Ophthalmology **6,** 89-95 (1995).
4. E. A. Swanson, D. Huang, M. R. Hee, J. G. Fujimoto, C. P. Lin, and C. A. Puliafito, "High-speed optical coherence domain reflectometry," Opt. Lett. **17,** 151-153 (1992).
5. J. Welzel, "Optical coherence tomography in dermatology: a review," Skin Research and Technology **7,** 1-9 (2001), <Go to ISI>://000166541600001.
6. B. H. Park, C. Saxer, S. M. Srinivas, and J. F. de Boer, "In vivo burn depth determination by high-speed fiber-based polarization sensitive optical coherence tomography," J. Biomed. Opt. **6,** 474-479 (2001).
7. M. C. Pierce, R. L. Sheridan, B. H. Park, B. Cense, and J. F. de Boer, "Collagen denaturation can be quantified in burned human skin using polarization-sensitive optical coherence tomography " Burns **30,** 511-517 (2004).
8. M. C. Pierce, J. Strasswimmer, B. H. Park, B. Cense, and J. F. de Boer, "Advances in optical coherence tomography imaging for dermatology " J. Invest. Dermatol. **123,** 458-463 (2004).
9. G. J. Tearney, M. E. Brezinski, B. E. Bouma, S. A. Boppart, C. Pitris, J. F. Southern, and J. G. Fujimoto, "In vivo endoscopic optical biopsy with optical coherence tomography," Science **276,** 2037-2039 (1997).
10. Z. Yaqoob, J. Wu, E. J. McDowell, X. Heng, and C. Yang, "Methods and application areas of endoscopic optical coherence tomography," J. Biomed. Opt. **11,** 063001 (2006).

#86494 - $15.00 USD Received 15 Aug 2007; revised 29 Oct 2007; accepted 30 Oct 2007; published 19 Dec 2007

11. M. V. J. Sivak, K. Kobayashi, J. A. Izatt, A. M. Rollins, R. Unq-Runyawee, A. Chak, R. C. Wong, G. A. Isenberg, and J. Willis, "High-resolution endoscopic imaging of the GI tract using optical coherence tomography," Gastrointest. Endosc. **51,** 474-479 (2000).
12. S. Brand, J. M. Poneros, B. E. Bouma, G. J. Tearney, C. C. Compton, and N. S. Nishioka, "Optical coherence tomography in the gastrointestinal tract," Endoscopy **32,** 796-803 (2000).
13. J. M. Poneros, S. Brand, B. E. Bouma, G. J. Tearney, C. C. Compton, and N. S. Nishioka, "Diagnosis of specialized intestinal metaplasia by optical coherence tomography," Gastroenterology **120,** 7-12 (2001).
14. B. E. Bouma, G. J. Tearney, C. C. Compton, and N. S. Nishioka, "High-resolution imaging of the human esophagus and stomach in vivo using optical coherence tomography," Gastrointest. Endosc. **51,** 467-474 (2000).
15. S. Jackle, N. Gladkova, F. Feldchtein, A. Terentieva, B. Brand, G. Gelikonov, V. Gelikonov, A. Segeev, A. Fritscher-Ravens, J. Freund, U. Seitz, S. Schroder, and N. Soehendra, "In vivo endoscopic optical coherence tomography of esophagitis, Barrett's esophagus, and adenocarcinoma of the esophagus," Endoscopy **32,** 750-755 (2000).
16. X. D. Li, S. A. Boppart, J. Van Dam, H. Mashimo, M. Mutinga, W. Drexler, M. Klein, C. Pitris, M. L. Krinsky, M. E. Brezinski, and J. G. Fujimoto, "Optical coherence tomography: advanced technology for the endoscopic imaging of Barrett's esophagus," Endoscopy **32,** 921-930 (2000).
17. H. Yabushita, B. E. Bouma, S. L. Houser, H. T. Aretz, I. K. Jang, K. H. Schlendorf, C. R. Kauffman, M. Shishkov, D. H. Kang, E. F. Halpern, and G. J. Tearney, "Characterization of human atherosclerosis by optical coherence tomography," Circulation **106,** 1640-1645 (2002).
18. O. A. Meissner, J. Rieber, B. G., M. Oswald, S. Reim, U. Siebert, T. Redel, M. Reiser, and U. Mueller-Lisse, "Intravascular optical coherence tomography: comparison with histopathology in atherosclerotic peripheral artery specimens," J. Vasc. Interv. Radiol. **17,** 343-349 (2006).
19. G. J. Tearney, I. K. Jang, and B. E. Bouma, "Optical coherence tomography for imaging the vulnerable plaque," J. Biomed. Opt. **11,** 021002 (2006).
20. F. I. Feldchtein, G. V. Gelikonov, V. M. Gelikonov, R. R. Iksanov, R. V. Kuranov, A. M. Sergeev, N. D. Gladkova, M. N. Ourutina, J. A. Warren Jr, and D. H. Reitze, "In vivo OCT imaging of hard and soft tissue of the oral cavity," Opt. Express **3,** 239-250 (1998).
21. A. V. Shakhov, A. B. Terentjeva, V. A. Kamensky, L. B. Snopova, V. M. Gelikonov, F. I. Feldchtein, and A. M. Sergeev, "Optical coherence tomography monitoring for laser surgery of laryngeal carcinoma," J. Surg. Oncol. **77,** 253-258 (2001).
22. B. J. Wong, J. R. P., S. Guo, J. M. Ridgway, U. Mahmood, J. Su, T. Y. Shibuya, R. L. Crumley, M. Gu, W. B. Armstrong, and Z. Chen, "In vivo optical coherence tomography of the human larynx: normative and benign pathology in 82 patients," Laryngoscope **115,** 1904-1911 (2005).
23. A. M. Klein, M. C. Pierce, S. M. Zeitels, R. R. Anderson, J. B. Kobler, M. Shishkov, and J. F. de Boer, "Imaging the human vocal folds in vivo with optical coherence tomography: a preliminary experience," Ann. Otol. Rhinol. Laryngol. **115,** 277-284 (2006).
24. E. V. Zagaynova, O. S. Streltsova, N. D. Gladkova, L. B. Snopova, G. V. Gelikonov, F. I. Feldchtein, and A. N. Morozov, "In vivo optical coherence tomography feasibility for bladder disease," J. Urol. **167,** 1492-1496 (2002).
25. G. J. Tearney, S. A. Boppart, B. E. Bouma, M. E. Brezinski, N. M. Weissman, J. F. Southern, and J. G. Fujimoto, "Scanning single-mode fiber optic catheter-endoscope for optical coherence tomography," Opt. Lett. **21,** 543-545 (1996).
26. B. E. Bouma and G. J. Tearney, "Power-efficient nonreciprocal interferometer and linear-scanning fiber-optic catheter for optical coherence tomography," Opt. Lett. **24,** 531-533 (1999).
27. V. X. D. Yang, M. L. Gordon, S.-j. Tang, N. E. Marcon, G. Gardiner, B. Qi, S. Bisland, E. Seng-Yue, S. Lo, J. Pekar, B. C. Wilson, and I. A. Vitkin, "High speed, wide velocity dynamic range Doppler optical coherence tomography (Part III): in vivo endoscopic imaging of blood flow in the rat and human gastrointestinal tracts," Opt. Express **11,** 2416-2424 (2003).
28. T. Mitsui, "Dynamic range of optical reflectometry with spectral interferometry," Japanese Journal of Applied Physics Part 1-Regular Papers Short Notes & Review Papers **38,** 6133-6137 (1999), <Go to ISI>://000083622000084.
29. R. Leitgeb, C. K. Hitzenberger, and A. F. Fercher, "Performance of fourier domain vs. time domain optical coherence tomography," Opt. Express **11,** 889-894 (2003).
30. J. F. de Boer, B. Cense, B. H. Park, M. C. Pierce, G. J. Tearney, and B. E. Bouma, "Improved singla-to-noise ratio in spectral-domain compared with time-domain optical coherence tomography," Opt. Lett. **28,** 2067-2069 (2003).
31. M. A. Choma, M. V. Sarunic, C. H. Yang, and J. A. Izatt, "Sensitivity advantage of swept source and Fourier domain optical coherence tomography," Opt. Express **11,** 2183-2189 (2003).
32. N. Nassif, B. Cense, B. H. Park, S. H. Yun, T. C. Chen, B. E. Bouma, G. J. Tearney, and J. F. de Boer, "In vivo human retinal imaging by ultrahigh-speed spectral domain optical coherence tomography," Opt. Lett. **29,** 480-482 (2004).
33. N. A. Nassif, B. Cense, B. H. Park, M. C. Pierce, S. H. Yun, B. E. Bouma, G. J. Tearney, T. C. Chen, and J. F. de Boer, "In vivo high-resolution video-rate spectral-domain optical coherence tomography of the human retina and optic nerve," Opt. Express **12,** 367-376 (2004).

#86494 - $15.00 USD Received 15 Aug 2007; revised 29 Oct 2007; accepted 30 Oct 2007; published 19 Dec 2007

34. S. H. Yun, G. J. Tearney, J. F. de Boer, N. Iftimia, and B. E. Bouma, "High-speed optical frequency-domain imaging," Opt. Express **11,** 2953-2963 (2003).
35. S. R. Chinn, E. A. Swanson, and J. G. Fujimoto, "Optical coherence tomography using a frequency-tunable optical source," Opt. Lett. **22,** 340-342 (1997).
36. M. A. Choma, K. Hsu, and J. A. Izatt, "Swept source optical coherence tomography using an all-fiber 1300-nm ring laser source," J. Biomed. Opt. **10,** 044009 (2005).
37. R. Huber, M. Wojtkowski, and J. G. Fujimoto, "Fourier Domain Mode Locking (FDML): A new laser operating regime and applications for optical coherence tomography," Opt. Express **14,** 3225-3237 (2006).
38. S. H. Yun, G. J. Tearney, B. J. Vakoc, M. Shishkov, W. Y. Oh, A. E. Desjardins, M. J. Suter, R. C. Chan, J. A. Evans, I. K. Jang, N. S. Nishioka, J. F. de Boer, and B. E. Bouma, "Comprehensive volumetric optical microscopy in vivo," Nat. Med. **12,** 1429-1433 (2006).
39. P. H. Tran, D. S. Mukai, M. Brenner, and Z. Chen, "In vivo endoscopic optical coherence tomography by use of a rotational microelectromechanical system probe," Opt. Lett. **29,** 1236-1238 (2004).
40. P. R. Herz, Y. Chen, A. D. Aguirre, K. Schneider, P. Hsiung, J. G. Fujimoto, K. Madden, J. Schmitt, J. Goodnow, and C. Peterson, "Micromotor endoscope catheter for in vivo, ultrahigh-resolution optical coherence tomography," Opt. Lett. **29,** 2261-2263 (2004).
41. X. Liu, M. J. Cobb, Y. Chen, M. B. Kimmey, and X. Li, "Rapid-scanning forward-imaging miniature endoscope for real-time optical coherence tomography," Opt. Lett. **29,** 1763-1765 (2004).
42. Y. T. Pan, H. K. Xie, and G. K. Fedder, "Endoscopic optical coherence tomography based on a microelectromechanical mirror," Opt. Lett. **26** 1966-1968 (2001).
43. A. Jain, A. Kopa, Y. T. Pan, G. K. Fedder, and H. K. Xie, "A two-axis electrothermal micromirror for endoscopic optical coherence tomography," IEEE J. Sel. Top. Quantum Electron. **10,** 636-642 (2004).
44. W. Jung, D. T. McCormick, J. Zhang, L. Wang, N. C. Tien, and Z. Chen, "Three-dimensional endoscopic optical coherence tomography by use of a two-axis microelectromechanical scanning mirror," Appl. Phys. Lett. **88,** 163901 (2006).
45. W. Jung, J. Zhang, L. Wang, P. Wilder-Smith, Z. Chen, D. T. McCormick, and N. C. Tien, "Three-dimensional optical coherence tomography employing a 2-axis microelectromechanical scanning mirror," IEEE J. Sel. Top. Quantum Electron. **11,** 806-810 (2005).
46. A. D. Aguirre, P. R. Hertz, Y. Chen, J. G. Fujimoto, W. Piyawattanametha, L. Fan, and M. C. Wu, "Two-axis MEMS scanning catheter for ultrahigh resolution three-dimensional and en face Imaging," Opt. Express **15,** 2445-2453 (2007).
47. J. T. W. Yeow, V. X. D. Yang, A. Chahwan, M. L. Gordon, B. Qi, I. A. Vitkin, B. C. Wilson, and A. A. Goldenberg, "Micromachined 2-D scanner for 3-D optical coherence tomography," Sens. Actuators A. **117,** 331-340 (2005).
48. J. M. Zara, and P. E. Patterson, "Polyimide amplified piezoelectric scanning mirror for spectral domain optical coherence tomography," Appl. Phys. Lett. **89,** 263901 (2006).
49. T. Mitsui, Y. Takahashi, and Y. Watanabe, "A 2-axis optical scanner driven nonresonantly by electromagnetic force for OCT imaging," J. Micromech. Microeng. **16,** 2482-2487 (2006).
50. B. H. Park, M. C. Pierce, B. Cense, S. H. Yun, M. Mujat, G. J. Tearney, B. E. Bouma, and J. F. de Boer, "Real-time fiber-based multi-functional spectral-domain optical coherence tomography at 1.3 um," Opt. Express **13,** 3931-3944 (2005).
51. J. A. Burns, S. M. Zeitels, R. R. Anderson, J. B. Kobler, M. C. Pierce, and J. F. de Boer, "Imaging the mucosa of the human vocal fold with optical coherence tomography " Ann. Otol. Rhinol. Laryngol. **114,** 671-676 (2005).

1. Introduction

Optical coherence tomography (OCT) is an optical imaging technique capable of cross-sectional imaging of biological tissues based on light scattering [1, 2]. Scattered light is resolved in depth using low coherence interferometry. With its high sensitivity, high resolution, and non-invasiveness, OCT has become a promising technique for *in vivo* clinical diagnosis in ophthalmology [2-4] and dermatology [5-8]. Development of scanning catheters has enabled endoscopic OCT imaging of internal organs and extended the OCT study field further [9, 10]. Endoscopic OCT imaging has demonstrated its ability to resolve layered tissue structures, and to differentiate normal from certain pathologic conditions within the esophagus [11-16], coronary artery [17-19] and other internal organs such as the oral cavity [20], larynx [21-23], and bladder [24].

Development of OCT catheters is critical for endoscopic OCT imaging. Conventional OCT catheters are composed of a single-mode optical fiber and small optical elements fused at the tip of the fiber to deflect and focus light onto a tissue [25-27]. This fiber assembly is housed in a flexible hollow shaft and can either translate or rotate by actuations at the

#86494 - $15.00 USD Received 15 Aug 2007; revised 29 Oct 2007; accepted 30 Oct 2007; published 19 Dec 2007

proximal end. For the imaging of tubular organs such as the gastrointestinal (GI) tract and vasculature, these catheters do circumferential scanning by rotation. These catheters are also used to image non-tubular organs by longitudinal translation [23, 26]. These conventional OCT catheters are small in size and flexible with their simple structure, and have been widely used for clinical studies. The recent development of spectral domain OCT (SD-OCT), or Fourier domain OCT (FD-OCT), has increased the sensitivity by orders of magnitude [28-31] which in turn has improved image acquisition speeds by more than an order of magnitude compared to conventional time domain OCT (TD-OCT) [32, 33]. Alternatively, the wavelength resolved interference fringes can be detected using high performance wavelength-swept light sources and is called optical frequency domain imaging (OFDI) or swept-source OCT [34-37]. These fast acquisition systems allow for high-speed endoscopic imaging. Conventional OCT catheters can be used for high-speed imaging of tubular organs, because their circumferential scanning can run at high speeds. Volumetric imaging of the esophagus and coronary artery was demonstrated by using an OCT catheter which rotates continuously with a rotary junction during slow longitudinal translation for 2D scanning [38]. However, for imaging non-tubular organs, conventional catheters scanning linearly are limited in scanning speed to a few frames/s due to various factors including large inertia, friction, and compliance related to proximal actuation. Furthermore, these translational catheters can only generate 2D images by scanning along a single axis. Therefore, the conventional OCT catheters are the limiting factor for high-speed 3D imaging of non-tubular organs.

Various OCT catheters have been developed such as side-looking vs. front-looking, proximal-actuated vs. distal-actuated, fine needle catheters etc [10]. Distal-actuated catheters are based on either miniaturized actuators [39-41] or microelectromechanical systems (MEMS) technology [42-49]. These catheters generally can scan in 2D for 3D imaging and can scan at high speeds. MEMS technology is especially promising to produce integrated miniaturized actuators for scanning catheters. MEMS-based scanning catheters have been developed with various actuation mechanisms such as electrothermal [42, 43], electrostatic [44-47], polyimide amplified piezoelectric [48], and magnetic [49] actuation. One-axis and two-axis electrothermal actuated scanners based on bimorph thermal actuator hinges have been implemented. Electrostatic actuated scanners are quite popular as they offer many advantages such as low mass, low power consumption, absence of exotic materials, and the possibility of built-in capacitive feedback. 2-axis electrostatic actuators using electrostatic comb-drive actuators demonstrated 3D tissue imaging [44-46]. However, these comb-drive actuators require small gaps and high driving voltages (~ 100V), with their potential failure becoming a concern for patient safety. The magnetically-actuated scanner can achieve large scanning ranges with low driving voltages across large gaps, which is advantageous for scanning catheters. A large size 2-axis magnetically-actuated scanner was implemented as a substitution for x-y galvanometric scanner pairs, not for endoscopic scanning catheters [49]. Distal-actuated catheters tend to be relatively large in size compared to the conventional OCT catheters, and most of the MEMS-based scanning catheters are at prototype stages.

In this work, we present a fully-assembled two-axis scanning catheter based on a magnetically-actuated MEMS micro-mirror scanner. This MEMS scanner can be actuated either statically or at its resonant frequency (>= 350Hz). Therefore, high-speed endoscopic OCT imaging is possible with this catheter. It has a scanning range of ± 20º in optical angle in both axes with low driving voltages (1~3 V). The assembled catheter measured 2.8 mm in outer diameter with a rigid body length of 12 mm. The design of the MEMS scanner, optical and mechanical design of the catheter, and *in vivo* 3D images of fingertips and oral cavity tissue taken with a multi-functional SD-OCT system are presented.

#86494 - $15.00 USD Received 15 Aug 2007; revised 29 Oct 2007; accepted 30 Oct 2007; published 19 Dec 2007

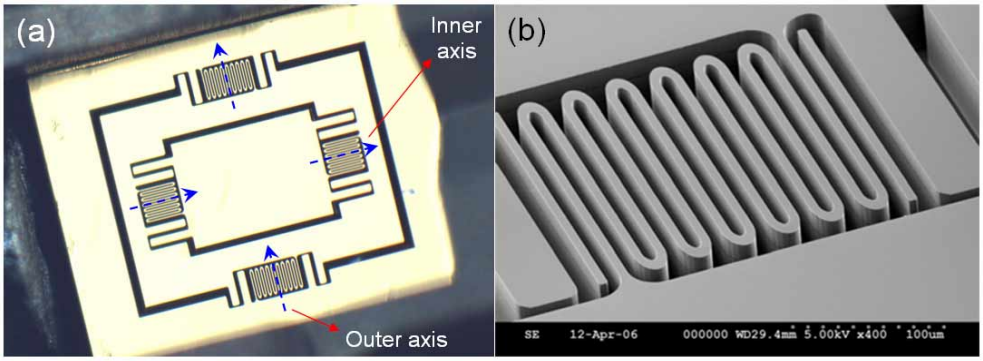

Fig. 1. The MEMS mirror scanner (a) and a SEM picture of a supporting folded flexure (b). A micro-mirror is supported by a 2-axis gimbal structure composed of folded flexure hinges and can deflect in two orthogonal axes: inner and outer axis depicted in the picture.

2. Catheter design and construction

2.1 MEMS mirror scanner

A photograph of the MEMS mirror scanner is shown in Fig. 1(a). A rectangular-shaped micro-mirror is mounted on a two-axis gimbal platform with folded flexure hinges. The micro-mirror can rotate in two axes: an inner axis along a pair of inner flexures and an orthogonal outer axis along the outer flexure pair. Dimensions of the mirror are 0.6 mm x 0.8 mm in width and height, respectively, and those of the whole unit are 2.4 mm x 2.9 mm. A scanning electron micrograph (SEM) picture of the folded flexure is shown in Fig. 1(b). Flexures are 6 microns wide and 50 microns deep, giving good out-of-plane stiffness. For magnetic actuation, a thin permanent magnet is glued to the back of the mirror and wire-wound coils are placed in the catheter body for each axis (refer to the section of catheter design for details).

A simple MEMS process (Fig. 2), composed of 2 photo-steps, was used to make the mirror scanner. The starting material was an SOI (Silicon On Insulator) wafer with a 50 μm thick SOI layer on a 350 μm thick handle wafer, with a 1 μm thick oxide layer in between (Fig. 2(a)). The mirrors and gimbals, including folded flexures, were formed by ICP (Inductively Coupled Plasma) etching in an STS reactor (STS plc, Newport, UK) (Fig. 2(b)). Following this step, the handle side was similarly patterned by ICP etching to free them (Fig. 2(c)). The exposed oxide was etched using buffered HF (BHF) (Fig. 2(d)). At this point, the mirrors were held in the wafer by thin tabs, which were broken to remove them from the wafer. Cr/Au was then sputtered on the mirror side of the chip (Fig. 2(d)). Thin magnet layers, which were composed of small NdFeB magnets, measuring 0.6 mm x 0.8 mm x 0.18 mm were glued to the backs of the mirrors manually (Fig. 2(e)). These small magnets were made by grinding magnet blanks to the desired thickness, dicing to the desired dimensions and then magnetizing. Reducing the mass of the mirror and magnet assembly was important to increase shock and vibration resistance and to limit mechanical resonance (Q factor). On the other hand, thicker magnet layers gave higher actuation torque for a given driving current, leading to a trade-off between actuation force and shock resistance. The rigidity of the folded flexures was set to balance between large scanning angles and mechanical stability. Resonant frequencies for the inner and outer axes were approximately 450 Hz and 350 Hz, respectively.

#86494 - $15.00 USD Received 15 Aug 2007; revised 29 Oct 2007; accepted 30 Oct 2007; published 19 Dec 2007

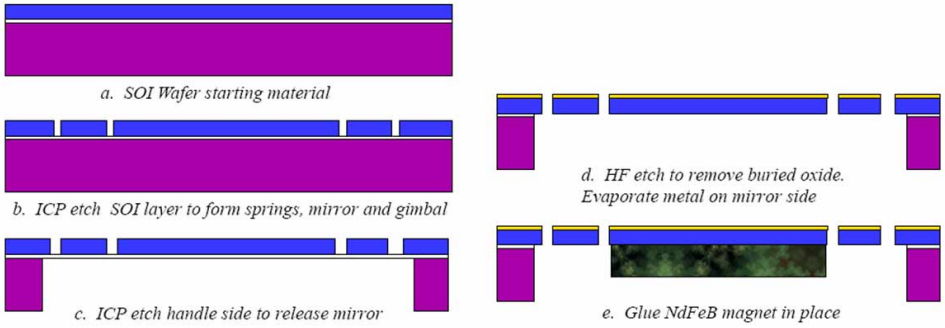

Fig. 2. MEMS scanner fabrication process

2.2 Catheter design

Figure 3 shows a cross-sectional schematic and corresponding photograph of the assembled catheter. In the schematic, the light path is shown in red. Light is delivered via a single mode optical fiber (Corning SMF-28, core diameter: 8.2 μm) from the left. The divergent beam from the fiber is focused by a GRIN lens (NSG America #ILH-0.70, 1.1 mm length, 0.51 mm focal length) and reflected down toward a MEMS mirror scanner with a fold mirror. The faces of the GRIN lens are angle-polished to avoid back reflection. The MEMS mirror reflects the beam up toward a specimen through a plano-convex cylindrical glass window. The glass window has anti-reflection (AR) coating on its surfaces. The beam focus is placed in the specimen, which is in contact with the catheter. The MEMS scanner redirects the beam in two orthogonal axes. Scattered light from the tissue returns back through the same optical path and is collected by the optical fiber. This configuration allows scanning of the beam forward and imaging close to the tip of the catheter. The glass window protects the MEMS scanner and keeps the cylindrical catheter shape. The scanning range is set to exclude normal incidence on the glass window in order to avoid strong back-reflections. The optical design was optimized via ZEMAX simulation (Zemax development corp., Bellevue, WA) to maintain image resolution throughout the 3D imaging region. The image resolution is approximately 25 microns at the Gaussian beam waist in transverse direction, and its Rayleigh range is approximately 1.5 mm in air (3 mm in depth of focus).

The catheter body was machined of titanium, since it is a strong, non-magnetic material. The rigid housing of the catheter is 2.8 mm in outer diameter with a length of 12 mm. A coil pair was placed under the mirror for magnetic actuation in the inner axis and a single coil was placed at the distal tip of the catheter for the actuation in the outer axis. Although very fine coils could be fabricated by lithography and electroplating, we decided to use wire-wound coils since they were commercially available at low costs. Coils were wound from a #50 AWG wire on temporary winding mandrels. The outer axis coils averaged approximately 390 turns and 35-40 ohms, whereas the smaller inner axis coil pairs averaged approximately 18 ohms. The inner axis coil pairs were mounted on titanium coil supports with small nubs to center the coils. These coil supports were glued to the main body using epoxy. The coils were painted with enamel (Testors Flat Black) to reduce stray light reflections from the body and its coupling to the optical fiber. For strain relief, the fine coil wires were brought out to a small flex circuit board with solder pads. Four #34 AWG multi-strand wires were used for external connection. Two leads were used for each axis of actuation.

As the final assembly step, a single mode optical fiber was attached to the catheter. The fiber was angle cleaved to avoid back-reflection from its tip and the fiber was aligned with the

#86494 - $15.00 USD Received 15 Aug 2007; revised 29 Oct 2007; accepted 30 Oct 2007; published 19 Dec 2007

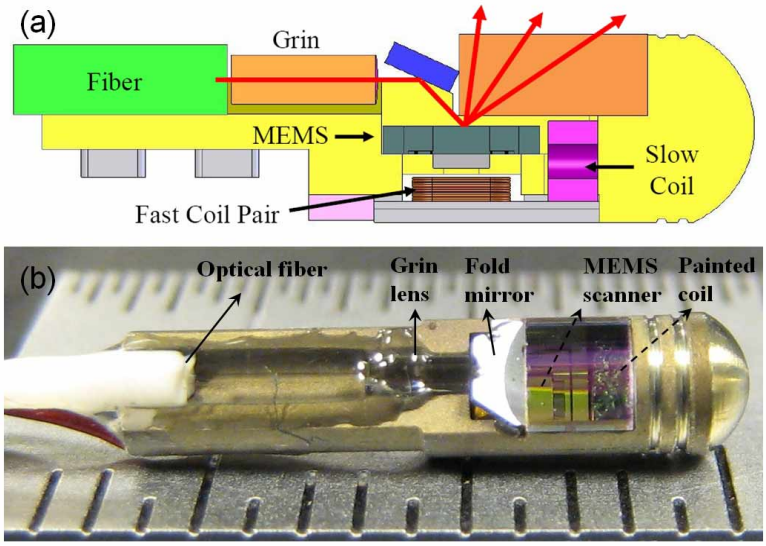

Fig. 3. Catheter schematic (a) and photograph (b). Light path is drawn in red in the schematic and light is redirected by the MEMS scanner. The catheter photograph was taken with a ruler underneath with millimeter unit. The optical fiber is glued to the catheter body with UV curing epoxy. The MEMS scanner appears in the photograph refracted by the plano-convex cylindrical window.

catheter body by using a precision 3D translator. The space between the fiber tip and the GRIN lens in the catheter was filled with ultraviolet (UV) curing epoxy (Norland 68) for index matching and gluing. It was important to set the distance between the fiber tip and the grin lens correctly as this distance determined the depth location of the beam focus in the sample. This distance was adjusted by imaging a sample of 5 μm diameter polystyrene microspheres embedded in agar gel with a pre-existing TD-OCT system such that the beam maintained focus throughout the entire imaging depth. Once this distance was set, the fiber was fixed in place by curing the epoxy with a UV gun.

2.3 Multi-functional SD-OCT system

The 2-axis MEMS scanning catheter was incorporated with a multi-functional SD-OCT system, capable of simultaneous intensity, polarization-sensitive (PS), and phase-resolved optical Doppler imaging [50]. Polarization-sensitive OCT (PS-OCT) enables depth-resolved measurement of light-polarization state changing properties of tissue, and has been used for applications including correlating burn depth with a decrease in birefringence [6], measuring the birefringence of the retinal nerve fiber layer, and monitoring the onset and progression of caries lesions by analyzing depth dependent changes in the polarization state of detected light. PS-OCT imaging is useful for endoscopic imaging of the vocal folds by providing additional contrast to resolve their layered structures [23, 51]. It may provide rheological information of the vocal folds based on the level of birefringence. Phase-resolved optical Doppler tomography enables depth-resolved imaging of flow by observing differences in phase of a spectral interferogram between successive depth scans. A detailed description of the system can be found in the literature [50]. The system is based on a fiber-based interferometer with a broadband light source centered at 1.3 μm with a bandwidth of 68 nm at full width half maximum (FWHM). This bandwidth gives the coherence length of 11.27 microns in air. The 2-axis scanning catheter in the sample arm is covered with a heat-shrink plastic sheath (FEP,

#86494 - $15.00 USD Received 15 Aug 2007; revised 29 Oct 2007; accepted 30 Oct 2007; published 19 Dec 2007

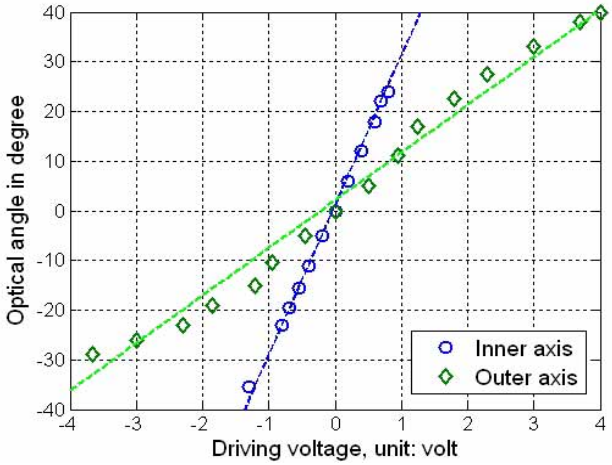

Fig. 4. Scanning range of the MEMS scanner. The lines are linear fits of measurement points.

Zeus Inc, Orangeburg, SC) and an epoxy glue is applied to its open end for sealing. Control signals for the MEMS scanner are generated by an acquisition computer and amplified by a power amplifier (PA74, Apex Microtech, Tucson, AZ) to provide enough electrical current (up to 100 mA) for driving the scanner. The acquisition speed is 18,500 axial scans per second.

3. Results

The scanning range of the MEMS scanner was measured at an intermediate assembly step, before the fold mirror and plano-convex cylindrical window were attached. A laser pointer was used to illuminate the scanner, and the spot positions vs. driving voltages were recorded using a paper screen with 1 mm spaced lines. Figure 4 shows optical angles of the MEMS scanner in both inner and outer axes vs. driving voltages. These angles scaled nearly linearly with the driving voltages in both axes and the angles higher than ± 30º were typically achieved with a voltage level of ± 1.2 V and ± 4 V for the inner and outer axis respectively. The electrical currents were calculated to be 50 mA and 100 mA for the inner and outer axis respectively by using their resistance values. The outer axis coil was relatively inefficient at applying torque compared to the inner axis coils due to a larger gap between the coil and the magnet on the back of the mirror. In the assembled catheter, the optical window refracted the beam, resulting in a slight nonlinearity in the deflection angle with the driving voltage due to thickness variations of the window. At large scan angles spurious vibrations at the mirror resonant frequency were observed. To avoid this vibration, the scan angle was reduced to approximately ± 20º optical angle for the inner axis and less than ± 30º optical angle for the outer axis. Image resolution was measured by imaging microspheres (5 microns in diameter) immobilized in agar. Full width at half maximum intensity (FWHM) in lateral direction measured approximately 23 μm on average.

In vivo 3D endoscopic imaging of tissues was performed by using the 2-axis scanning catheters and the multifunctional SD-OCT system. Consecutive cross-sectional images were acquired by using either the inner axis or the outer axis as the fast scanning axis and the other axis as the slow scanning axis. The scanning in the fast axis was driven by a sinusoidal waveform (18.5 Hz) to make sure that the scanner followed the driving waveform without distortion. The scanning in the slow axis was driven by a linear triangular waveform (0.09

#86494 - $15.00 USD Received 15 Aug 2007; revised 29 Oct 2007; accepted 30 Oct 2007; published 19 Dec 2007

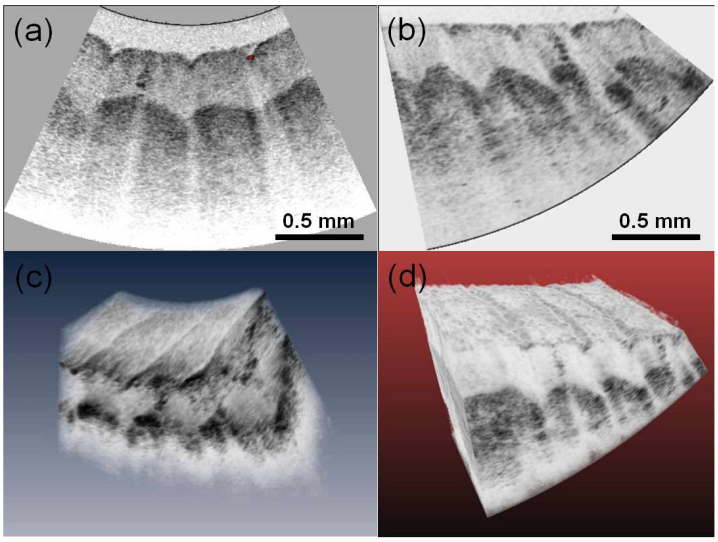

Fig. 5. In vivo finger tip images: cross-sectional images in the inner axis (a) and outer axis (b) respectively, and 3D reconstructed images (c, d) based on the consecutive cross-sectional images in (a) and (b) respectively.

Hz). Each cross-sectional image was taken during a full cycle of the sinusoidal waveform in the fast axis and was composed of 1024 axial scans. The cross-sectional image was symmetric with the first half in the forward scanning direction and the second half in the opposite (backward) direction. 100 consecutive cross-sectional images were acquired by scanning in the slow axis. A post image processing was performed in Matlab (Mathworks, MA) to generate images and its steps are following: (1) A standard SD-OCT image processing algorithm was applied first to obtain both intensity and PS images. (2) Each cross-sectional image, which contained both forward and backward images, was split into two images and incoherently averaged to reduce speckle noise. (3) The cross-sectional images were rescaled linearly in angle by interpolation of the sinusoidal driving waveform in the fast axis. The resulting images are in polar coordinates. (4) The images in polar coordinates were converted into Cartesian coordinates by a secondary interpolation step.

First, human fingertips were imaged *in vivo* and their 3D images are presented in Fig. 5. Figures 5(a) and 5(b) are cross-sectional images. In Fig. 5(a), the cross-sectional images were acquired by using the inner axis of the scanner as the fast axis with a driving voltage of ± 0.8V. The boundary of the cross-sectional images reflects the radial geometry and the large angle (± 20˚) of the scan. Its scanning range was approximately 1 mm in length on the surface. The slow (outer) axis was driven with ± 1V and its scanning range was 0.55 mm in length on the surface. 100 consecutive cross-sectional images were acquired. The total acquisition time was 5.4 seconds. In Fig. 5(b), the fast and slow scanning axes were switched from the one in Fig 5(a): the outer axis was used as the fast scanning axis and the inner axis as the slow axis. In this configuration, the scanning range of approximately 1.5 mm was achieved in the fast axis (outer) and 1 mm was for the slow (inner) axis. The driving voltage was ± 2.8 V and ± 0.8 V for the outer and inner axis respectively. These intensity images were displayed with an inverse gray-scale such that black indicates the highest intensity and white the lowest. Both cross-sectional images visualized the finger tip structures: the layered structures of the thick epithelium and dermis from superficial to deep, wrinkled fingerprint patterns, and sweat ducts in the epithelium. Figures 5(c) and 5(d) show 3D reconstructions of the consecutive cross-sectional images in Figs. 5(a) and 5(b). They visualize the 3D tissue

#86494 - $15.00 USD Received 15 Aug 2007; revised 29 Oct 2007; accepted 30 Oct 2007; published 19 Dec 2007

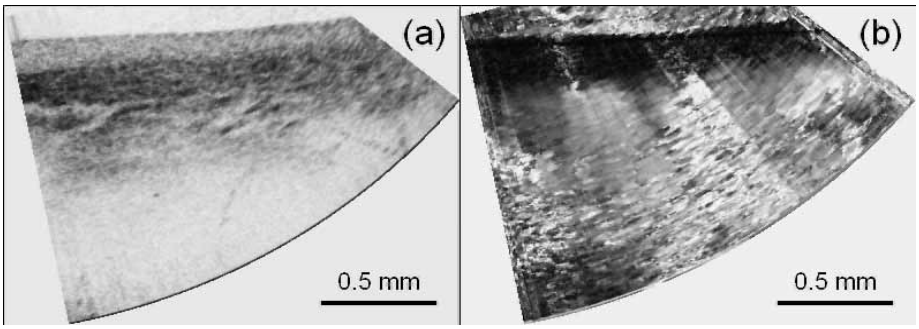

Fig. 6. Movie of cross-sectional images of internal oral cavity *in-vivo*. Intensity image (a) and polarization sensitive (PS) image (b) are updated with the cross-section advancing in the orthogonal axis. The intensity image shows layered structures of epithelium and glands from superficial to deep, and the PS image shows no birefringence in the epithelium and some birefringence in the glands

structures including the fingerprint orientation.

Next as a demonstration of *in vivo* endoscopic imaging of internal tissues, oral cavity tissues were imaged. 3D imaging was performed by using the outer axis as the fast scanning axis and the inner axis as the slow, in order to obtain a large scanning range: 1.5 mm and 1.0 mm on the surface for the fast and slow axis respectively. 100 consecutive images were acquired with the imaging speed of 18.5 frames/s and the total imaging time was 5.4 seconds. Both intensity and PS images were acquired simultaneously. Consecutive cross-sectional images of both intensity and PS were processed as a movie (Fig. 6). The cross-sectional image shows the oral tissue structures: from the surface to deep, epithelium, a layer of well developed glands, and amorphous layer with some sparse large vessels. The gland layer appeared thin, because the catheter was pressed hard onto the tissue in order to be held stationary during acquisition time and the tissue was squeezed. The PS images display accumulated phase retardation from the surface, where black indicates 0º phase retardation and white 180º. Further accumulation of phase retardation wraps back around to a black color. The epithelium layer stayed in black with no birefringence and in the layer below the epithelium, the color changed from black to white, indicating some birefringence. Scrambling of black and white at the bottom of the images indicated un-determined polarization states (or noise regime).

4. Summary and discussion

We have shown the implementation of a 2-axis MEMS scanning catheter actuated by magnetic field for endoscopic SD-OCT imaging. The fabrication of the micro-mirror MEMS scanner and optical and mechanical design of the catheter were presented. Although magnetic actuation required separate wired coils, small coils were produced and the assembled catheter measured only 2.8 mm in outer diameter. A disadvantage of the small size catheter was that its scanning length decreased with the reduction of outer diameter given a fixed scanning angle. Resonant vibration of the scanner was observed at high deflection angles when both axes were actuated, which limited the scanning range. However, it had approximately 1 mm scanning length in both axes. The causes of such vibration is not clear: it may be possibly attributed to nonlinear response to driving voltages, coupling between rotations in two axes, or misalignment between the magnetic fields of the wired coil pairs for the inner axis at large rotational angles. We are trying to resolve this issue in the next generation catheter design. Magnetic actuation requires low voltages (1~3 V), but with somewhat large currents. The power consumed in the catheter was estimated to be 150 mW by driving both axes. The

#86494 - $15.00 USD Received 15 Aug 2007; revised 29 Oct 2007; accepted 30 Oct 2007; published 19 Dec 2007

temperature of the catheter body was measured to be approximately 45 ˚C due to small body size and thin electrical wires. Better heat sinking may be required for larger scanning ranges in the next generation catheter. Additional metal wires can be connected to the catheter body for heat dissipation and to provide some mechanical rigidity which is necessary for catheter operation. Power consumption can be reduced by moving the coils closer to the mirror.

The catheter was used for *in vivo* endoscopic tissue imaging by incorporation with the multi-functional SD-OCT system. In principle, this catheter is ready for clinical study of endoscopic tissue imaging, such as the human vocal folds. The next step will be to image the vocal folds of anaesthetized patients in the operating room.

Acknowledgments

The technical development of this work was sponsored by NIH-NCRR 19768 and CIMIT, the Center for the Integration of Medicine and Innovative Technology with funding from the Department of the Army under its Cooperative Agreement DAMD17-02-2-0006 to Massachusetts General Hospital and lower tier subcontract to The Charles Stark Draper Laboratory.

The content of the information does not necessarily reflect the position or the policy of the Government, and no official endorsement should be inferred.

#86494 - $15.00 USD Received 15 Aug 2007; revised 29 Oct 2007; accepted 30 Oct 2007; published 19 Dec 2007